ACS APPLIED MATERIALS & INTERFACES

Research Article

www.acsami.org

Hierarchical Mesoporous/Macroporous Perovskite $La_{0.5}Sr_{0.5}CoO_{3-x}$ Nanotubes: A Bifunctional Catalyst with Enhanced Activity and Cycle Stability for Rechargeable Lithium Oxygen Batteries

Guoxue Liu,[†] Hongbin Chen,[†] Lu Xia,[†] Suqing Wang,*[,†] Liang-Xin Ding,[†] Dongdong Li,[†,‡] Kang Xiao,[†] Sheng Dai,[‡] and Haihui Wang*[,†,‡]

[†]School of Chemistry and Chemical Engineering, South China University of Technology, Guangzhou 510640, China

[‡]School of Chemical Engineering, The University of Adelaide, Adelaide, SA 5005, Australia

Supporting Information

ABSTRACT: Perovskites show excellent specific catalytic activity toward both oxygen reduction reaction (ORR) and oxygen evolution reaction (OER) in alkaline solutions; however, small surface areas of the perovskites synthesized by traditional sol–gel methods lead to low utilization of catalytic sites, which gives rise to poor Li–O_2 batteries performance and restricts their application. Herein, a hierarchical mesporous/macroporous perovskite $La_{0.5}Sr_{0.5}CoO_{3-x}$ (HPN-LSC) nanotube is developed to promote its application in Li–O_2 batteries. The HPN-LSC nanotubes were synthesized via electrospinning technique followed by postannealing. The as-prepared HPN-LSC catalyst exhibits outstanding intrinsic ORR and OER catalytic activity. The HPN-LSC/KB electrode displays excellent performance toward both discharge and charge processes for Li–O_2 batteries, which enhances the reversibility, the round-trip efficiency, and the capacity of resultant batteries. The synergy of high catalytic activity and hierarchical mesoporous/macroporous nanotubular structure results in the Li–O_2 batteries with good rate capability and excellent cycle stability of sustaining 50 cycles at a current density of 0.1 mA cm^{-2} with an upper-limit capacity of 500 mAh g^{-1}. The results will benefit for the future development of high-performance Li–O_2 batteries using hierarchical mesoporous/macroporous nanostructured perovskite-type catalysts.

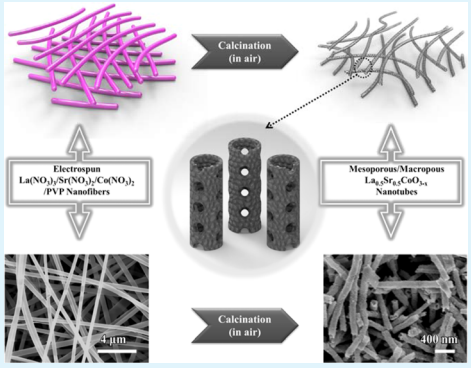

KEYWORDS: *electrospinning, perovskites, hierarchical mesoporous/macroporous nanotubes, bifunctional catalysts, lithium–oxygen batteries*

1. INTRODUCTION

Rechargeable lithium–oxygen (Li–O_2) batteries can provide a high theoretical energy density of 11 680 Wh·kg^{-1}, which is close to the energy density of gasoline (~13 000 Wh·kg^{-1}), and are expected to be potential to replace state-of-the-art lithium-ion batteries (~300 Wh·kg^{-1}) for electronic devices, such as electronic vehicles (EV)/hybrid electric vehicles (HEV), consumer electronics, electricity grid, and renewable energy storage.[1−6] However, the realistic application of Li–O_2 batteries has been restricted by several serious challenges, including high overvoltage, poor rate capacity, and short cycle life, which are mainly due to the sluggish dynamics of the oxygen electrode during the Li_2O_2 formation ($2Li^+ + O_2 \rightarrow Li_2O_2$, oxygen reduction reaction, ORR) and the Li_2O_2 decomposition ($Li_2O_2 \rightarrow 2Li^+ + O_2$, oxygen evolution reaction, OER).[4,7−10] A desirable cathodic catalyst for Li–O_2 batteries should be a highly efficient bifunctional one which possesses excellent catalytic activity toward both ORR and OER.

Perovskites, ABO_3-type oxides, are considered as promising catalysts in various catalytic reactions,[11−15] mainly due to their low cost, high electrochemical stability, high electronic/ionic conductivity, and the remarkable structured capability to control a wide range of doping and substituting elements.[16,17] Moreover, the perovskite oxides have been regarded as a bifunctional catalyst because of excellent specific catalytic activity toward ORR and OER in alkaline solutions.[18−20] The perovskite oxides, such as $Sr_{0.95}Ce_{0.05}CoO_{3-x}$, $LaNi_{1-x}Mg_xO_3$, $LaNi_{1-x}Fe_xO_3$, $La_{0.8}Sr_{0.2}MnO_3$, $La_{1.7}Ca_{0.3}Ni_{0.75}Cu_{0.25}O_4$, Sr_2CrMoO_{6-x}, etc., have been explored as potential cathodic catalyst candidates for Li–O_2 batteries.[21−26] Unfortunately, most perovskites synthesized via the traditional sol–gel approach are usually in micrometer-scale together with a nonporous structure which shows low surface area (below 5 m^2 g^{-1}), leading to low utilization of catalytic sites.[18−27] Recent studies have indicated that porous nanostructured perovskites, such as $La_{0.75}Sr_{0.25}MnO_3$ nanotubes,[28] 3DOM $LaFeO_3$,[29] etc., can supply more catalytic sites than nonporous materials. The porous nanostructure can also store the reaction products and decrease the undesirable clogging of the oxygen electrodes, which would improve cycle stability performance. However,

Received: July 20, 2015
Accepted: September 29, 2015
Published: September 29, 2015

DOI: 10.1021/acsami.5b06587
ACS Appl. Mater. Interfaces 2015, 7, 22478−22486

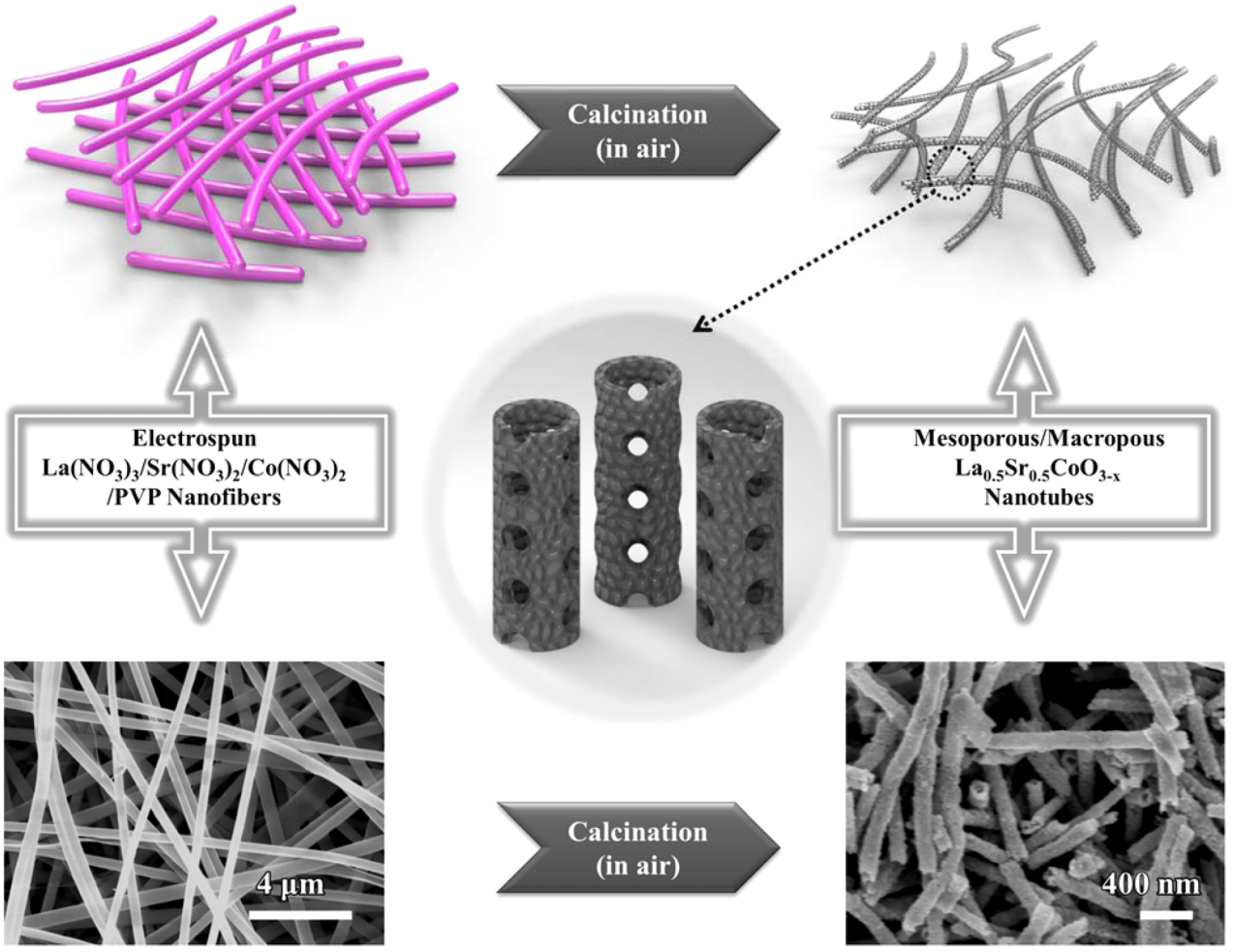

Figure 1. Schematic illustration of the synthetic strategy of hierarchical mesoporous/macroporous $La_{0.5}Sr_{0.5}CoO_{3-x}$ nanotubular catalysts for rechargeable Li−O_2 batteries.

most of them displayed the performance with a large overpotential. Among various perovskites, $La_{0.5}Sr_{0.5}CoO_{3-x}$ has excellent oxygen mobility, extraordinarily high conductivity, and good catalytic activities, which have exhibited excellent performance in solid oxide fuel cells (SOFCs).[30−33] Moreover, $La_{0.5}Sr_{0.5}CoO_{3-x}$ possesses unique intrinsic catalytic activity for ORR/OER in alkaline media among the perovskite-type oxides.[18,19,34,35] Recently, the Mai group reported hierarchical mesoporous perovskite $La_{0.5}Sr_{0.5}CoO_{2.91}$ nanowires as bifunctional catalysts, which show a high capacity of ∼11 000 mAh g^{-1} and 25 cycles with an upper-limit capacity stability.[34,36] The mesoporous (∼12 nm) structured materials can provide plenty of catalytic sites, but the small pores are easily clogged by Li_2O_2 product, leading to loss of catalytic activity and poor cycle stability.[37] Some researchers have evaluated that the macroporous structure can better store Li_2O_2 product than mesoporous structure and is not impeded by reaction products.[37−40] More importantly, both a low overpotential and good cycle stability are essential to realize application of Li−O_2 batteries. Therefore, a hierarchical mesoporous/macroporous structured bifunctional catalyst is proposed to enhance performance of Li−O_2 batteries.

Herein, we developed hierarchical mesoporous/macroporous $La_{0.5}Sr_{0.5}CoO_{3-x}$ nanotubes as the bifunctional (ORR/OER) catalyst for Li−O_2 batteries, which was prepared by a facile electrospining technique following calcination. Metal nitrate and polymer were dissolved in *N*,*N*-dimethylformamide (DMF), the mixture was electrospun to nanofibers, and the final nanotubes with hierarchical pores were obtained after calcination in air (Figure 1). The resulting hierarchical mesoporous/macroporous $La_{0.5}Sr_{0.5}CoO_{3-x}$ nanotubes have the following advantages: (i) high surface areas with both mesopores and macropores which can provide more contact for electrolyte-electrode, more active sites for ORR/OER during Li−O_2 batteries operation, and more space to store discharged products; (ii) direct current pathways that can facilitate electron transport contrasted with nonporous bulk catalyst; (iii) short O_2^{2-}/Li^+ diffusion lengths that can improve ion transferring rates to oxygen electrode. Therefore, it can be expected that this hierarchical architectural $La_{0.5}Sr_{0.5}CoO_{3-x}$ will benefit the overall electrochemical performance of Li−O_2 batteries. When it is used for the cathodic catalyst, Li−O_2 batteries exhibit a high specific discharge capacity of 5799 mAh cm^{-2} at 0.1 mA cm^{-2}, good rate capacity, and long cycle stability.

2. EXPERIMENTAL SECTION

2.1. Materials. $La(NO_3)\cdot 6H_2O$ (≥99.0% purity), $Sr(NO_3)_2$ (≥99.0% purity), $Co(NO_3)_2\cdot 6H_2O$ (≥99.0% purity), polyvinylpyrrolidone (PVP, ≥99.0% purity, Mw ≈ 1 300 000), *N*,*N*-dimethylformamide (DMF, AR), TEGDME (≥99.0% purity), Lithium bis(trifluoromethanesulfonyl)imide (LiTFSI, 99.9% purity), polyvinylidene difluoride (PVDF, 99.9% purity), *N*-methyl-2-pyrrolidinone (NMP,

DOI: 10.1021/acsami.5b06587
ACS Appl. Mater. Interfaces 2015, 7, 22478−22486

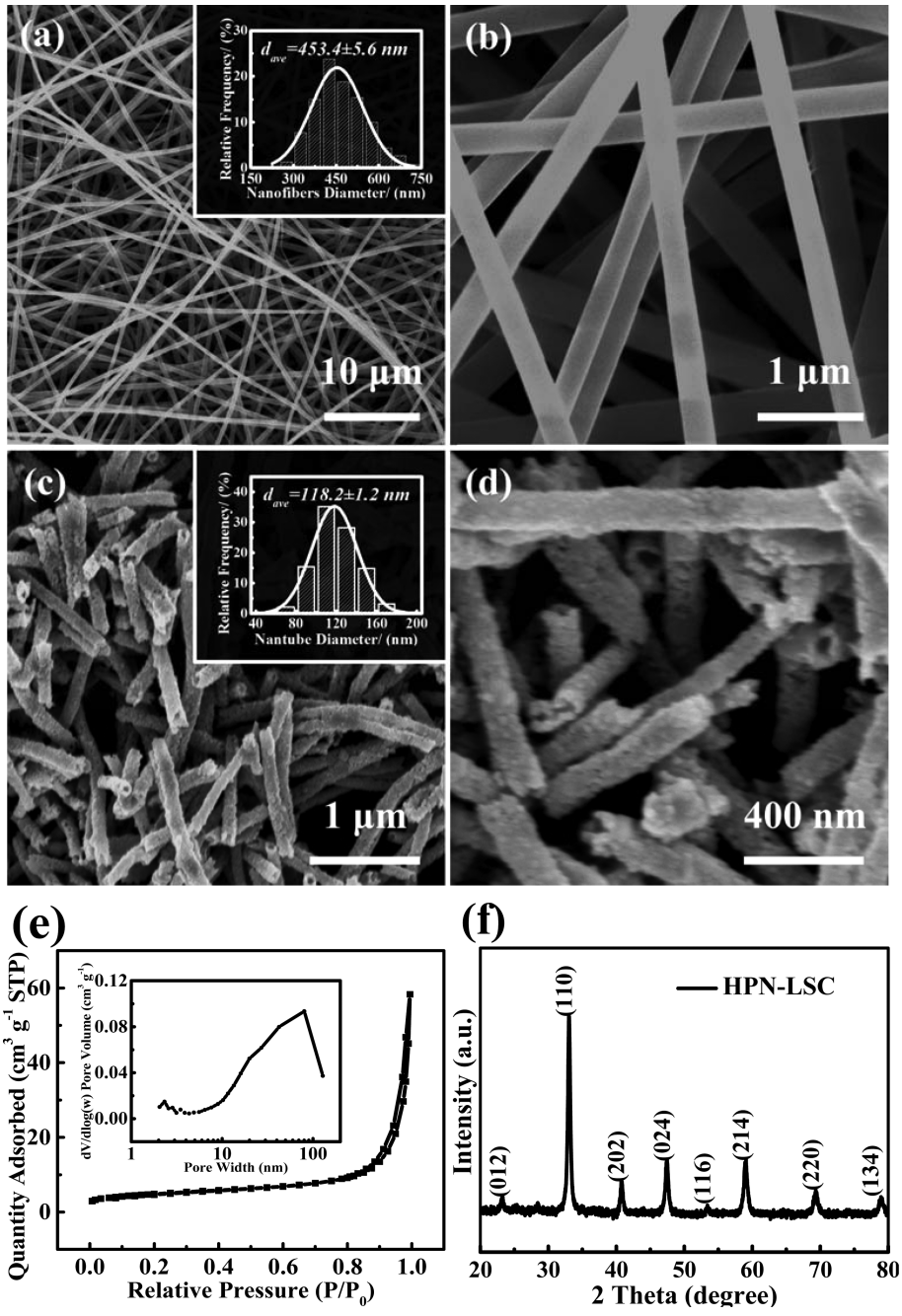

Figure 2. FESEM images at different magnifications. (a, b) As-obtained electrospun composite nanofibers. Inset of (a) shows diameter distribution histogram of the nanofibers. (c, d) HPN-LSC after thermal treatment at 750 °C for 3 h in air. Inset of (c) shows diameter distribution histogram of HPN-LSC. (e) Nitrogen adsorption−desorption isotherms and pore size distribution (inset of (e)) of HPN-LSC (f) XRD patterns of HPN-LSC.

AR), and Ketjenblack carbon were purchased from Aladdin Reagent (Aladdin Industrial Corporation).

2.2. Synthesis of Hierarchical Mesoporous/Macroporous $La_{0.5}Sr_{0.5}CoO_{3-x}$ Nanotubes. Hierarchical mesoporous/macroporous $La_{0.5}Sr_{0.5}CoO_{3-x}$ nanotubes were prepared via an electrospinning method following heat treatment. In a typical experiment, desired amount of $La(NO_3)\cdot 6H_2O$, $Sr(NO_3)_2$, $Co(NO_3)_2\cdot 6H_2O$, and polyvinylpyrrolidone (PVP) were dissolved in *N*,*N*-dimethylformamide (DMF). The mixture was stirred for 12 h at room temperature, and a transparent purple-colored solution was obtained. The solution was transferred to a 5 mL plastic syringe attached to 20-gauge stainless steel spinneret. A voltage of 20 kV was applied to the spinneret. The electrospining fibers were collected on the target aluminum foil, which was fixed at 20 cm away from the spinneret tip. The electrospun process was performed at ∼45 °C and a humidity of 20−30%. The obtained nanofibers were dried at 60 °C for 6 h under vacuum, and then the dried nanofibers were sintered at 750 °C for 3 h with a heating rate of 1 °C min^{-1} in air.

2.3. Characterization. The morphologies and structures of samples were characterized by field-emission scanning electron microscopy (FESEM, NOVA NANOSEM 430), transmission electron microscopy (TEM, JEM-2100F), X-ray diffraction (XRD, Bruker D8 Advance), nitrogen adsorption−desorption measurement (Micromeritics ASAP 2010), X-ray photoelectron spectroscopy (XPS analysis, ESCALAB 250 spectrometer), and Raman spectroscopy (HJY LabRAM Aramis).

2.4. Li−O_2 Battery Measurements. The electrochemical properties of Li−O_2 batteries were carried out assembling a 2032-type coin cell in a glovebox with Ar atmosphere. The HPN-LSC/KB electrodes (oxygen electrode) were fabricated by coating the homogeneous slurry

DOI: 10.1021/acsami.5b06587
ACS Appl. Mater. Interfaces 2015, 7, 22478−22486

on the Ni foam, composed of 60% Ketjenblack carbon (KB), 30% hierarchical mesoporous/macroporous nanotube $La_{0.5}Sr_{0.5}CoO_{3-x}$ catalyst (HPN-LSC), and 10% polyvinylidene difluoride (PVDF) in *N*-methyl-2-pyrrolidone (NMP). The electrodes were dried at 80 °C for 12 h under vacuum. The mass load of the carbon on the electrodes was 0.5 ± 0.1 mg_{carbon} cm^{-2}, and the mass load of the catalyst on the electrodes is about 0.25 $mg_{catalyst}$ cm^{-2}. The established Li−O_2 cells included an oxygen electrode, a glass fiber membrane separator, a Li metal foil as the counter electrode and the anode, and 1 M LiTFSI in tetraethylene glycol dimethyl ether (TEGDME) as the electrolyte. The galvanostatical discharge and charge tests of the Li−O_2 cells were performed by a battery testing system at room atmosphere within a voltage window of 2.20−4.35 V (versus Li/Li^+) after a 5 h rest period. Cyclic voltammetry tests were measured at a rate of 0.1 mV s^{-1} within the potential range of 2.20−4.35 V (versus Li/Li^+) by an electrochemical workstation (IM 6ex).

2.5. Rotating Disk Electrode Tests. An amount of 5 mg of HPN-LSC was mixed with 1 mg of KB in 1 mL of ethanol added to 100 μL of Nafion solution, followed by sonication for 60 min to form a homogeneous solution. A saturated calomel electrode was used as the reference electrode, a platinum foil was used as the counter electrode, and the working electrode was a glassy carbon rotating disk electrode (RDE) with a diameter of 5 mm. An amount of 10 μL of the above-prepared solution was adhered to the RDE and slowly dried to form a thin film working electrode. In the calculation process, all potential should be +0.990 V in 0.1 M KOH solution versus the reversible hydrogen electrode (RHE). All potential values ($E - iR$) are iR-corrected to compensate for the effect of solution resistance, where i is the current and R is the uncompensated ohmic electrolyte resistance (~45 Ω) measured via high frequency ac impedance in O_2-saturated 0.1 M KOH. Details kinetic analysis is described in Supporting Information.

3. RESULTS AND DISCUSSION

The morphologies of the nanofiber precursors and the synthesized HPN-LSC catalysts were observed by a field-emission scanning electron microscopy (FESEM), as shown in Figure 2. The nanofiber precursors show a smooth surface with an average diameter of 453.4 ± 5.6 nm, ranging from 300 to 600 nm (inset of Figure 2a). A tubular nanostructure was obtained after being sintered at 750 °C in air for 3 h (Figure 2c,d). The average outer diameter of the resulting HPN-LSC is around 118.2 ± 1.2 nm with a uniformly narrow distribution (inset of Figure 2c). Furthermore, some small pores on the surface of the nanotubes can be observed on the HPN-LSC surface (Figure 2d), which is caused by the generated gases associated with the decomposition of metal nitrate and polymer during calcination. The existence of small pores is also demonstrated by nitrogen adsorption−desorption measurements, as shown in Figure 2e. The broad pore size distribution (inset of Figure 2e) of the HPN-LSC indicates that the catalyst possesses mesopores and macropores. The Brunauer−Emmett−Teller (BET) specific surface area of the HPN-LSC is found to be 17.18 m^2 g^{-1}, which is much larger than that of the perovskites prepared by traditional methods.[18−20,27] X-ray diffraction (XRD) patterns (Figure 2f) were used to elucidate the crystalline structure of the obtained HPN-LSC. All diffraction peaks can be assigned to well-crystallized perovskite oxides (JCPDS = Joint Committee on Powder Diffraction Standards; JCPDS card no. 00-048-0122), indicating the successful synthesis of the perovskite LSC55. The transmission electron microscopy (TEM) image further presents the porous tubular morphology of the HPN-LSC with typical surface pores marked using white arrows in Figure 3a. Moreover, the TEM image also shows that the tubular $La_{0.5}Sr_{0.5}CoO_{3-x}$ (LSC55) is constituted by various nanoparticles with their sizes ranging

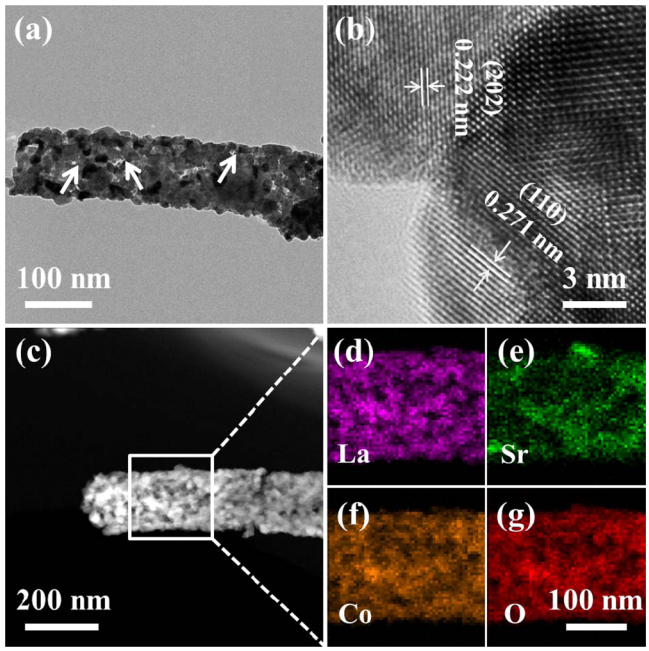

Figure 3. (a) TEM image, (b) HRTEM image, and (c) HAADF-STEM image of HPN-LSC. (d−g) EDS elemental mappings (lanthanum (La), strontium (Sr), cobalt (Co), and oxygen (O)) of the area marked in (c).

from 15 to 50 nm (Figure S1). Meanwhile, the high-resolution TEM (HRTEM) image (Figure 3b) further confirms the formation of the perovskite structure. The *d*-spacings of lattice fringes are 0.222 and 0.271 nm corresponding to the (202) and (110) planes of the LSC55 perovskite, which are in agreement with previously reported XRD patterns. Figure 3c−g displays the TEM image and elemental distribution mappings of a typical HPN-LSC nanotube by energy-dispersive X-ray spectroscopy (EDS), which suggests that all elements (La, Sr, Co, and O) in the HPN-LSC are homogeneously dispersive. From materials characterization, it is evident that the hierarchical mesoporous/macroporous nanotubular $La_{0.5}Sr_{0.5}CoO_{3-x}$ perovskite catalyst is successfully prepared.

Rotating disk electrode (RDE) techniques were used to investigate the ORR and OER intrinsic catalytic activities of the HPN-LSC catalyst in an O_2-saturated 0.1 M KOH electrolyte. To evaluate the kinetic performance for the ORR activity of the HPN-LSC catalyst, the ORR polarization curves of the HPN-LSC with a sweep rate of 5 mV s^{-1} under different rotation rates from 400 to 2025 rpm are displayed in Figure 4a. The Koutecky−Levich (K-L) plots (Figure 4b) evaluated from the above ORR polarization curves of HPN-LSC present good linearity. The corresponding electron transfer number n estimated from the K-L plots is ~4 at 0.40−0.50 V (versus RHE), implying a four-electron oxygen reduction process on the HPN-LSC catalyst in 0.1 M KOH solution, similar to the commercial Pt/C catalyst.[21,41] The ORR polarization curves of glassy carbon, KB, and HPN-LSC are shown in Figure 4c. The HPN-LSC catalyst exhibits a more positive onset potential than that of most perovskite oxides, such as $LaNiO_3$, $Ba_{0.5}Sr_{0.5}Co_{0.8}Fe_{0.2}O_{3-x}$, and $La_{0.8}Sr_{0.2}MnO_3$.[42−44] Figure 4d presents the OER polarization curves of glassy carbon, KB, and HPN-LSC. The OER onset potential of HPN-LSC (1.48 V versus RHE/0.25 V overpotential) is lower than that of the $Ba_{0.5}Sr_{0.5}Co_{0.8}Fe_{0.2}O_{3-x}$ catalyst (1.55 V versus RHE/0.30 V

DOI: 10.1021/acsami.5b06587
ACS Appl. Mater. Interfaces 2015, 7, 22478−22486

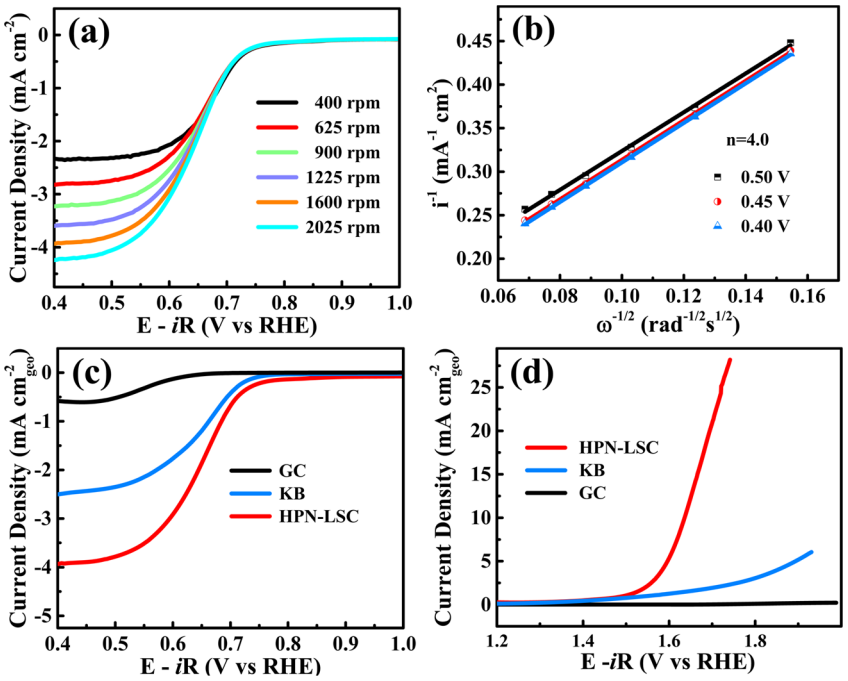

Figure 4. (a) ORR polarization curves of the HPN-LSC catalyst in O_2-saturated 0.1 M KOH with a sweep rate of 5 mV s^{-1} under different rotation rates. (b) Koutecky–Levich plots of the HPN-LSC catalyst based on the ORR polarization curves at 0.40, 0.45, and 0.50 V. (c) ORR and (d) OER polarization curves of glassy carbon (GC), KB, and HPN-LSC catalyst at same measurement condition.

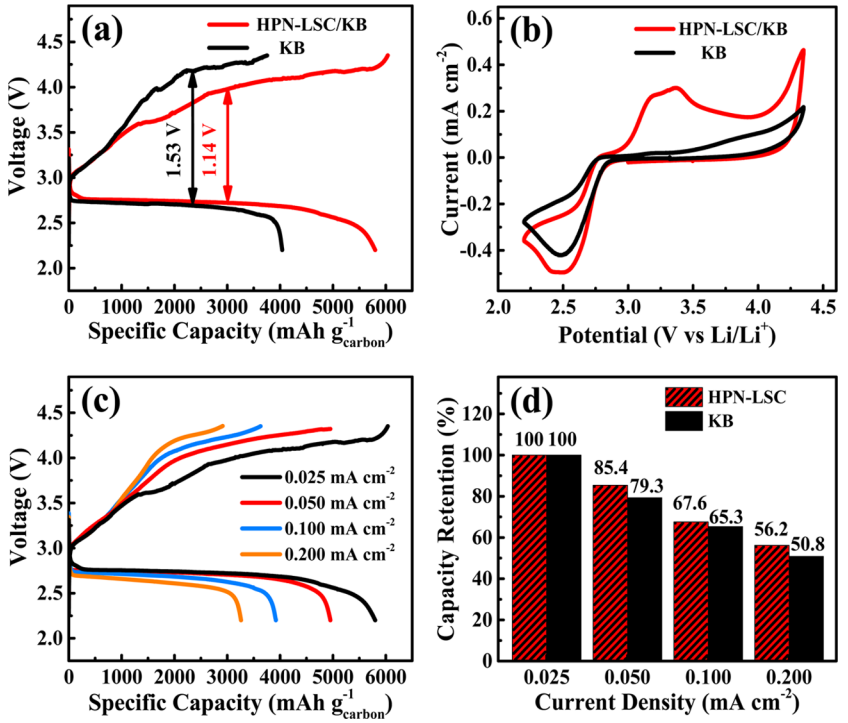

Figure 5. (a) First discharge/charge curves of Li–O_2 batteries with HPN-LSC/KB and KB electrode at a current density of 0.025 mA cm^{-2}. (b) CV curves of HPN-LSC/KB and KB electrodes between 2.20 and 4.35 V at 0.1 mV s^{-1}. (c) Galvanostatic discharge/charge curves of Li–O_2 batteries with the HPN-LSC/KB electrode at various current densities. (d) Capacity retention of the two kinds of electrodes at different current densities.

overpotential) which is one of the highest OER intrinsic activity among perovskites.[18,45,46] Remarkably, the combined overpotentials from both ORR and OER of the HPN-LSC can be about 0.71 V, which is comparable to the best intrinsic activity of the bifunctional oxides (~0.70 V) in the literature.[47] These results demonstrate that the fabricated HPN-LSC is an excellent bifunctional oxygen electrocatalyst, showing both excellent ORR and OER catalytic capability.

The electrochemical performance of the HPN-LSC/KB electrode and that of the pure KB electrode were further investigated in Li–O_2 batteries. The structure of a rechargeable Li–O_2 battery with the HPN-LSC catalyst and the working

DOI: 10.1021/acsami.5b06587
ACS Appl. Mater. Interfaces 2015, 7, 22478–22486

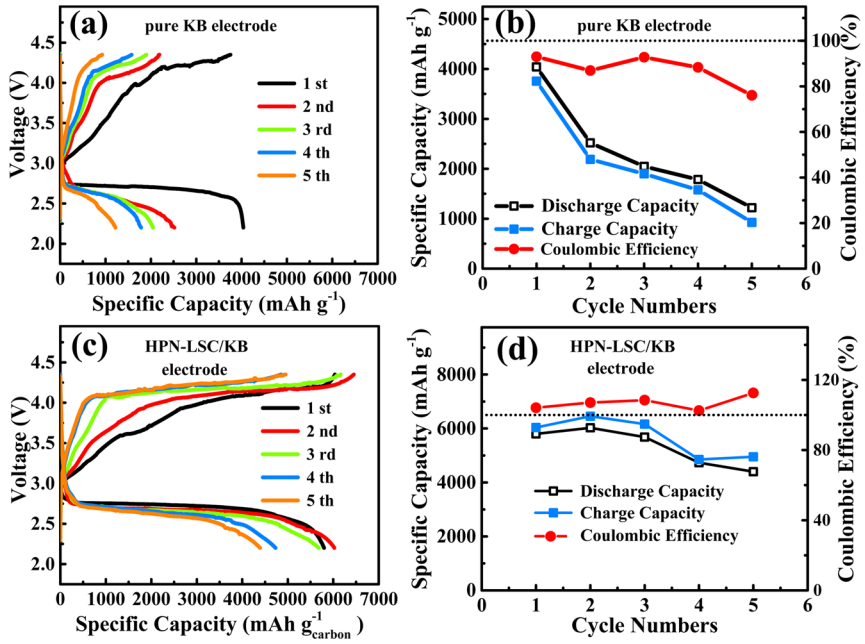

Figure 6. (a) Cyclic performance, discharge/charge specific capacity, and (b) Coulombic efficiency of Li−O_2 batteries with HPN-LSC/KB electrode at a current density of 0.025 mA cm^{-2}. (c) Cyclic performance, discharge/charge specific capacity, and (d) Coulombic efficiency of Li−O_2 batteries with pure KB electrode at a current density of 0.025 mA cm^{-2}.

mechanism of the oxygen electrode containing HPN-LSC are elucidated in Figure S2. Although the bulk resistivity of $La_{0.5}Sr_{0.5}CoO_{3-x}$ (3.16×10^{-4} Ω cm) is much lower than that of many metal oxides, such as $LaMnO_3$ (1.6 or 0.63 Ω cm), $La_{0.9}Sr_{0.1}MnO_3$ (0.82 Ω cm), and $La_{0.78}Sr_{0.18}Mn_{0.97}O_3$ (8.9×10^{-2} Ω cm), it is still higher than that of Ketjenblack carbon (1×10^{-4} Ω cm).[32,48] In addition, Ketjenblack carbon with a large specific surface area can provide the space to store the Li_2O_2 product. The Ketjenblack carbon with good electronic conductivity and large specific surface area is added to the oxygen cathode to improve its conductivity and capability for Li_2O_2 storage. The HPN-LSC catalyst with high ORR and OER activity is used to promote the formation and the decomposition of Li_2O_2 in the oxygen cathode. During discharge process, lithium ion reacts with reduced oxygen forming Li_2O_2 (ORR), which is deposited on the oxygen electrode; during charge process, the reaction products of Li_2O_2 are decomposed into lithium ion and oxygen (OER). Figure 5a shows the first charge−discharge curves of pure KB electrode and the HPN-LSC/KB electrode measured between 2.20 and 4.35 V at a current density of 0.025 mA cm^{-2}. The average discharge voltage plateau of Li−O_2 batteries with the HPN-LSC/KB electrode is about 2.73 V (versus Li^+/Li), which is higher than that of pure KB electrode (2.67 V). Especially, the charge voltage plateau of Li−O_2 batteries with the HPN-LSC/KB electrodes is about 3.87 V (versus Li^+/Li), which is much lower than that of pure KB electrode (4.20 V). The Li−O_2 batteries with the addition of HPN-LSC catalyst (1.14 V) consequently exhibit lower overvoltage than the batteries with pure KB (1.53 V). The round-trip efficiency of the Li−O_2 batteries with HPN-LSC/KB electrodes is ~70.5%, higher than the 63.6% for pure KB electrodes. These results clearly indicate that the HPN-LSC catalyst has high catalytic activity toward both OER and ORR processes for Li−O_2 batteries. That can be further confirmed by the cyclic voltammetry (CV) study (Figure 5b). Compared with pure KB electrode, the HPN-LSC/KB electrode exhibits higher ORR/OER onset potential and much larger ORR/OER peak current density. The improved battery capacity in the presence of the HPN-LSC catalyst is also evident in Figure 5a, where the HPN-LSC/KB electrode exhibits the first discharge capacity of 5799 mAh g^{-1} and pure KB electrode only gives 4041 mAh g^{-1}. In addition, the first charge capacity of HPN-LSC/KB is also very high (5799 mAh g^{-1}, 100% of initial discharge capacity), indicating that the HPN-LSC catalyst offers highly reversible recharge characteristics. For comparison, pure KB electrode exhibits relatively low initial charge capacities of 3750 mAh g^{-1} (93% of initial discharge capacity). Figure 5c shows the discharge/charge curves of the Li−O_2 batteries with the HPN-LSC/KB electrode at various current densities. With the increase in current density, the discharge capacity of the HPN-LSC/KB electrode drops. However, the HPN-LSC/KB electrode displays higher discharge capacities than that of pure KB electrode (Figure S3) at different current densities. In addition, the capacity retention rate of the HPN-LSC/KB electrode is still 56.8% at 0.2 mA cm^{-2}, which is higher than that of KB (50.8%) (Figure 5d). The higher specific capacity and better rate capability performance of the HPN-LSC/KB electrode can be attributed to its high ORR/OER catalytic activity and porous nanotubular structure.[28,47]

The cycling operations of the Li−O_2 batteries with and without the presence of the HPN-LSC catalyst were examined. Figure 6 presents the cycling performance of the Li−O_2 batteries at a current density of 0.025 mA cm^{-2} over a voltage window from 2.20 to 4.35 V. The HPN-LSC/KB electrode shows much better cycle stability than that of pure KB electrode. The HPN-LSC/KB electrode exhibits a high specific capacity of 5799 mAh g^{-1} for the initial discharge, and its discharge capacity keeps at 4391 mAh g^{-1} after five cycles. The capacity retention is 75.7% with a 100% Coulombic efficiency. On the other hand, pure KB electrode shows a specific capacity of 4041 mAh g^{-1} for the initial discharge and the capacity decreases to 1234 mAh g^{-1} after five cycles. The capacity retention is only 30% with an 80% Coulombic efficiency.

DOI: 10.1021/acsami.5b06587
ACS Appl. Mater. Interfaces 2015, 7, 22478−22486

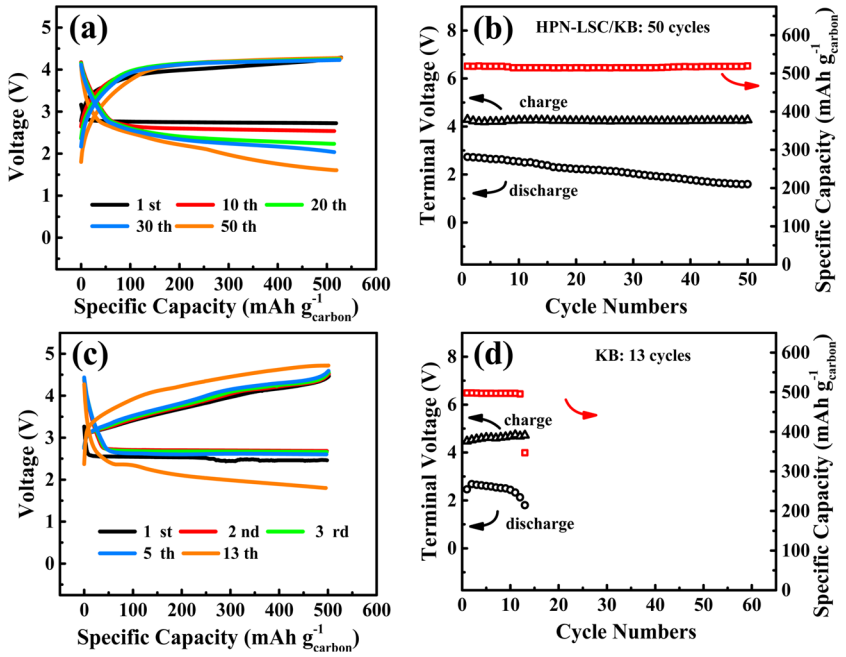

Figure 7. Cyclic performance of Li−O_2 batteries with HPN-LSC/KB electrodes (a, b) and pure KB electrodes (c, d) electrodes at a current density of 0.1 mA cm^{-2} with an upper-limit capacity of 500 mAh g^{-1}. (a, c) Discharge/charge curves at different cycles. (b, d) Discharge capacity and terminal voltage of discharge/charge against cycle numbers.

Comparisons on the XPS and Raman spectra of the HPN-LSC/KB electrodes after discharge and charge are shown in Figures S4 and S5, which can be used to indicate the reversible formation and decomposition of Li_2O_2 associated with the discharge and charge processes.[49] A weak Li_2CO_3 peak is evidenced in the XPS spectra, which suggests trace amount of Li_2CO_3 is generated due to the unstable carbon materials and unavoidable electrolyte decomposition.[50] The improved cycling stability should be associated with the stable hierarchical mesoporous/macroporous nanotubular structure of the HPN-LSC catalyst.[28,38,47]

In order to further investigate the influence of hierarchical mesoporous/macroporous nanotubular structure on battery cycling stability, the morphologies of pure KB electrode and HPN-LSC/KB electrode after initial discharge were observed by SEM (Figure S6c,d). The surface of pure KB electrode is tightly covered by the insulated Li_2O_2 products, which will hinder Li^+ (or O_2) charge transfer inside the electrode during the cycling processes, and thus the capacity of pure KB electrode dramatically decays after five cycles. By contrast, the HPN-LSC/KB electrode is not fully covered by Li_2O_2. The existing channels on electrode surface facilitate oxygen and electron transfer, which could enhance the decomposition of Li_2O_2 during the following charge process. The morphologies of pure KB electrode and the HPN-LSC/KB electrode are also examined after first charging in Figure S6e,f. Residual Li_2O_2 on pure KB electrodes can be observed, but there are almost no Li_2O_2 products on the HPN-LSC/KB electrodes. That indicates that Li_2O_2 can be fully decomposed during the charge processes for the HPN-LSC/KB electrode, and the HPN-LSC catalysts exhibit high OER catalytic activity to decompose Li_2O_2 associated with the charging process. The interaction of excellent catalytic activity and hierarchical mesoporous/macroporous nanotubular structure of the HPN-LSC is beneficial to Li_2O_2 formation and decomposition on the oxygen electrode, which results in the outstanding cycling performance of the Li−O_2 batteries.

The cycling performances of the Li−O_2 batteries were further examined at a current density of 0.1 mA cm^{-2} with a limit capacity of 500 mAh g^{-1}, as shown Figure 7. The voltage drop on discharge process from 4.0 to 2.7 V is caused by the ohmic resistance of the batteries and the overpotential of the surface reaction of $2Li^+ + O_2 \rightarrow Li_2O_2$.[9] The Li−$O_2$ batteries with the HPN-LSC/KB electrode can maintain 50 cycles (Figure 7a,b). On the contrary, the Li−O_2 batteries with pure KB electrode only sustain 13 cycles (Figure 7c,d). The results further imply that the HPN-LSC catalyst can effectively improve cycling stability, and the HPN-LSC/KB electrode is the potential oxygen electrode with an excellent performance of Li−O_2 batteries. Compared to the previous results (Table S1), it is confirmed that the hierarchical mesoporous/macroporous nanotubular perovskite-type LSC55 catalyst in this study is a competitive electrochemical catalyst among the perovskite-type catalysts for rechargeable Li−O_2 batteries.

4. CONCLUSION

In summary, a hierarchical mesoporous/macroporous perovskite-type $La_{0.5}Sr_{0.5}Co_{3-x}$ nanotubular catalyst (HPN-LSC) was successfully fabricated by a simple electrospining technique and employed as a bifunctional catalyst for Li−O_2 batteries. The HPN-LSC catalyst shows high intrinsic ORR and OER catalytic activity and an overpotential (0.71 V) in 0.1 M KOH solution. The HPN-LSC/KB electrode also presents excellent ORR and OER catalytic activity with a low overvoltage (1.14 V) during the discharge and charge processes for Li−O_2 batteries and thus improves the round-trip efficiency. Besides, the fabricated Li−O_2 batteries using the HPN-LSC/KB electrodes exhibit a high specific capacity of 5799 mAh g^{-1} and good rate capability, as well as a superior cycling life with low charge voltage. The excellent Li−O_2 batteries performance can be attributed to the synergistic effect of the high catalytic activity and the stable

DOI: 10.1021/acsami.5b06587
ACS Appl. Mater. Interfaces 2015, 7, 22478−22486

hierarchical mesoporous/macroporous nanotubular structure of the perovskite-type HPN-LSC. In addition, this work provides a widely new strategy to develop highly efficient catalysts for Li–O_2 batteries through design of bifunctional (ORR/OER) perovskite-type catalysts with mesoporous/macroporous nanostructure.

■ ASSOCIATED CONTENT

Supporting Information

The Supporting Information is available free of charge on the ACS Publications website at DOI: 10.1021/acsami.5b06587.

Details of kinetic analysis; TEM image, HRTEM image, and histogram of diameter distributions of the synthesized HPN-LSC; the structure of a rechargeable Li–O_2 battery with HPN-LSC catalysts and the working mechanism of the oxygen electrode containing HPN-LSC; discharge/charge profiles of Li–O_2 batteries with pure KB electrode at various current densities; XPS spectra, Raman spectra and SEM images of HPN-LSC/KB electrode and pure KB electrode before first discharge, after first discharge, and after first charge; and comparison of electrochemical performance between the current work and micrometer-scale or nanoscale structured catalysts for Li–O_2 batteries (PDF)

■ AUTHOR INFORMATION

Corresponding Authors

*S.W.: e-mail, cesqwang@scut.edu.cn.
*H.W.: e-mail, hhwang@scut.edu.cn.

Notes

The authors declare no competing financial interest.

■ ACKNOWLEDGMENTS

The authors greatly acknowledge the financial support by National Science Fund for Distinguished Young Scholars of China (Grant 21225625), Natural Science Foundation of China (Grant 21576100), Nature Science Foundation of Guangdong (Grant 2014A030312007), and the Australian Research Council (ARC) through the Future Fellow Program (Grant FT140100757).

■ REFERENCES

(1) Bruce, P. G.; Freunberger, S. A.; Hardwick, L. J.; Tarascon, J. M. Li-O_2 and Li-S Batteries with High Energy Storage. *Nat. Mater.* **2012**, *11*, 19–29.

(2) Abraham, K. M.; Jiang, Z. A Polymer Electrolyte-Based Rechargeable Lithium/Oxygen Battery. *J. Electrochem. Soc.* **1996**, *143*, 1–5.

(3) Gao, X. P.; Yang, H. X. Multi-electron Reaction Materials for High Energy Density Batteries. *Energy Environ. Sci.* **2010**, *3*, 174–189.

(4) Girishkumar, G.; McCloskey, B.; Luntz, A. C.; Swanson, S.; Wilcke, W. Lithium-Air Battery: Promise and Challenges. *J. Phys. Chem. Lett.* **2010**, *1*, 2193–2203.

(5) Grande, L.; Paillard, E.; Hassoun, J.; Park, J. B.; Lee, Y. J.; Sun, Y. K.; Passerini, S.; Scrosati, B. The Lithium/Air Battery: Still an Emerging System or a Practical Reality? *Adv. Mater.* **2015**, *27*, 784–800.

(6) Cheng, F.; Liang, J.; Tao, Z.; Chen, J. Functional Materials for Rechargeable Batteries. *Adv. Mater.* **2011**, *23*, 1695–1715.

(7) Kraytsberg, A.; Ein-Eli, Y. Review on Li-Air Batteries-Opportunities, Limitations and Perspective. *J. Power Sources* **2011**, *196*, 886–893.

(8) Li, F.; Zhang, T.; Zhou, H. Challenges of Non-aqueous Li-O_2 Batteries: Electrolytes, Catalysts, and Anodes. *Energy Environ. Sci.* **2013**, *6*, 1125–1141.

(9) Luntz, A. C.; McCloskey, B. D. Nonaqueous Li-Air Batteries: A Status Report. *Chem. Rev.* **2014**, *114*, 11721–11750.

(10) Freunberger, S. A.; Chen, Y.; Drewett, N. E.; Hardwick, L. J.; Bardé, F.; Bruce, P. G. The Lithium-Oxygen Battery with Ether-Based Electrolytes. *Angew. Chem., Int. Ed.* **2011**, *50*, 8609–8613.

(11) Luo, H.; Klande, T.; Cao, Z.; Liang, F.; Wang, H. H.; Caro, J. A CO_2-Stable Reduction-tolerant Nd-containing Dual Phase Membrane for Oxyfuel CO_2 Capture. *J. Mater. Chem. A* **2014**, *2*, 7780–7787.

(12) Jiang, H.; Wang, H. H.; Werth, S.; Schiestel, T.; Caro, J. Simultaneous Production of Hydrogen and Synthesis Gas by Combining Water Splitting with Partial Oxidation of Methane in a Hollow-Fiber Membrane Reactor. *Angew. Chem., Int. Ed.* **2008**, *47*, 9341–9344.

(13) Wang, H. H.; Cong, Y.; Yang, W. High Selectivity of Oxidative Dehydrogenation of Ethane to Ethylene in an Oxygen Permeable Membrane Reactor. *Chem. Commun.* **2002**, *14*, 1468–1469.

(14) Jiang, H.; Wang, H. H.; Liang, F.; Werth, S.; Schiestel, T.; Caro, J. Direct Decomposition of Nitrous Oxide to Nitrogen by in Situ Oxygen Removal with a Perovskite Membrane. *Angew. Chem., Int. Ed.* **2009**, *48*, 2983–2986.

(15) Lee, D. U.; Park, H. W.; Park, M. G.; Ismayilov, V.; Chen, Z. Synergistic Bifunctional Catalyst Design Based on Perovskite Oxide Nanoparticles and Intertwined Carbon Nanotubes for Rechargeable Zinc-Air Battery Applications. *ACS Appl. Mater. Interfaces* **2015**, *7*, 902–910.

(16) Jung, K. N.; Jung, J. H.; Im, W. B.; Yoon, S.; Shin, K. H.; Lee, J. W. Doped Lanthanum Nickelates with a Layered Perovskite Structure as Bifunctional Cathode Catalysts for Rechargeable Metal-Air Batteries. *ACS Appl. Mater. Interfaces* **2013**, *5*, 9902–9907.

(17) Liao, Q.; Wang, Y.; Chen, Y.; Wei, Y.; Wang, H. H. Novel Bifunctional Tantalum and Bismuth Co-doped Perovskite Ba-$Bi_{0.05}Co_{0.8}Ta_{0.15}O_{3-\delta}$ with High Oxygen Permeation. *J. Membr. Sci.* **2014**, *468*, 184–191.

(18) Suntivich, J.; May, K. J.; Gasteiger, H. A.; Goodenough, J. B.; Yang, S. H. A Perovskite Oxide Optimized for Oxygen Evolution Catalysis from Molecular Orbital Principles. *Science* **2011**, *334*, 1383–1385.

(19) Suntivich, J.; Gasteiger, H. A.; Yabuuchi, N.; Nakanishi, H.; Goodenough, J. B.; Yang, S. H. Design Principles for Oxygen-Reduction Activity on Perovskite Oxide Catalysts for Fuel Cells and Metal-Air Batteries. *Nat. Chem.* **2011**, *3*, 546–550.

(20) Vojvodic, A.; Nørskov, J. K. Optimizing Perovskites for the Water-Splitting Reaction. *Science* **2011**, *334*, 1355–1356.

(21) Zhang, D.; Song, Y.; Du, Z.; Wang, L.; Li, Y.; Goodenough, J. B. Active $LaNi_{1-x}Fe_xO_3$ Bifunctional Catalysts for Air Cathodes in Alkaline Media. *J. Mater. Chem. A* **2015**, *3*, 9421–9426.

(22) Jung, K. N.; Lee, J. I.; Im, W. B.; Yoon, S.; Shin, K. H.; Lee, J. W. Promoting Li_2O_2 Oxidation by an $La_{1.7}Ca_{0.3}Ni_{0.75}Cu_{0.25}O_4$ Layered Perovskite in Lithium-Oxygen Batteries. *Chem. Commun.* **2012**, *48*, 9406–9408.

(23) Yang, W.; Salim, J.; Li, S.; Sun, C.; Chen, L.; Goodenough, J. B.; Kim, Y. Perovskite $Sr_{0.95}Ce_{0.05}CoO_{3-\delta}$ Loaded with Copper Nanoparticles as a Bifunctional Catalyst for Lithium-Air Batteries. *J. Mater. Chem.* **2012**, *22*, 18902–18907.

(24) Ma, Z.; Yuan, X.; Li, L.; Ma, Z. F. The Double Perovskite Oxide $Sr_2CrMoO_{6-\delta}$ as an Efficient Electrocatalyst for Rechargeable Lithium Air Batteries. *Chem. Commun.* **2014**, *50*, 14855–14858.

(25) Du, Z.; Yang, P.; Wang, L.; Lu, Y.; Goodenough, J. B.; Zhang, J.; Zhang, D. Electrocatalytic Performances of $LaNi_{1-x}Mg_xO_3$ Perovskite Oxides as Bi-functional Catalysts for Lithium Air Batteries. *J. Power Sources* **2014**, *265*, 91–96.

(26) Fu, Z.; Lin, X.; Huang, T.; Yu, A. Nano-sized $La_{0.8}Sr_{0.2}MnO_3$ as Oxygen Eeduction Catalyst in Nonaqueous Li/O_2 Batteries. *J. Solid State Electrochem.* **2012**, *16*, 1447–1452.

(27) Suntivich, J.; Gasteiger, H. A.; Yabuuchi, N.; Yang, S. H. Electrocatalytic Measurement Methodology of Oxide Catalysts Using a

DOI: 10.1021/acsami.5b06587
ACS Appl. Mater. Interfaces 2015, 7, 22478–22486

Thin-Film Rotating Disk Electrode. *J. Electrochem. Soc.* **2010**, *157*, B1263−B1268.
(28) Xu, J. J.; Xu, D.; Wang, Z. L.; Wang, H. G.; Zhang, L. L.; Zhang, X. B. Synthesis of Perovskite-Based Porous $La_{0.75}Sr_{0.25}MnO_3$ Nanotubes as a Highly Efficient Electrocatalyst for Rechargeable Lithium-Oxygen Batteries. *Angew. Chem., Int. Ed.* **2013**, *52*, 3887−3890.
(29) Xu, J. J.; Wang, Z. L.; Xu, D.; Meng, F. Z.; Zhang, X. B. 3D Ordered Macroporous $LaFeO_3$ as Efficient Electrocatalyst for Li-O_2 Batteries with Enhanced Rate Capability and Cyclic Performance. *Energy Environ. Sci.* **2014**, *7*, 2213−2219.
(30) Leonard, D. N.; Kumar, A.; Jesse, S.; Biegalski, M. D.; Christen, H. M.; Mutoro, E.; Crumlin, E. J.; Yang, S. H.; Kalinin, S. V.; Borisevich, A. Y. Nanoscale Probing of Voltage Activated Oxygen Reduction/Evolution Reactions in Nanopatterned $(La_xSr_{1-x})CoO_{3-\delta}$ Cathodes. *Adv. Energy Mater.* **2013**, *3*, 788−797.
(31) Liu, J. M.; Ong, C. K. The Large Magnetoresistance Property of $La_{0.5}Sr_{0.5}CoO_{3-x}$ Thin Films Prepared by Pulsed Laser Deposition. *Appl. Phys. Lett.* **1998**, *73*, 1047−1049.
(32) Miyahara, Y.; Miyazaki, K.; Fukutsuka, T.; Abe, T. Catalytic Roles of Perovskite Oxides in Electrochemical Oxygen Reactions in Alkaline Media. *J. Electrochem. Soc.* **2014**, *161*, F694−F697.
(33) Wang, Y.; Fan, H. J. Low-Field Magnetoresistance Effect in Core-Shell Structured $La_{0.7}Sr_{0.3}CoO_3$ Nanoparticles. *Small* **2012**, *8*, 1060−1065.
(34) Zhao, Y.; Xu, L.; Mai, L.; Han, C.; An, Q.; Xu, X.; Liu, X.; Zhang, Q. Hierarchical Mesoporous Perovskite $La_{0.5}Sr_{0.5}CoO_{2.91}$ Nanowires with Ultrahigh Capacity for Li-air Batteries. *Proc. Natl. Acad. Sci. U. S. A.* **2012**, *109*, 19569−19574.
(35) Grimaud, A.; Carlton, C. E.; Risch, M.; Hong, W. T.; May, K. J.; Yang, S. H. Oxygen Evolution Activity and Stability of $Ba_6Mn_5O_{16}$, $Sr_4Mn_2CoO_9$, and $Sr_6Co_5O_{15}$: The Influence of Transition Metal Coordination. *J. Phys. Chem. C* **2013**, *117*, 25926−25932.
(36) Shi, C.; Feng, J.; Huang, L.; Liu, X.; Mai, L. Reaction Mechanism Characterization of $La_{0.5}Sr_{0.5}CoO_{2.91}$ Electrocatalyst for Rechargeable Li-Air Battery. *Int. J. Electrochem. Sci.* **2013**, *8*, 8924−8930.
(37) Xie, J.; Yao, X.; Cheng, Q.; Madden, I. P.; Dornath, P.; Chang, C. C.; Fan, W.; Wang, D. Three Dimensionally Ordered Mesoporous Carbon as a Stable, High-Performance Li-O_2 Battery Cathode. *Angew. Chem., Int. Ed.* **2015**, *54*, 4299−4303.
(38) Guo, Z.; Zhou, D.; Dong, X. L.; Qiu, Z.; Wang, Y.; Xia, Y. Ordered Hierarchical Mesoporous/Macroporous Carbon: A High-Performance Catalyst for Rechargeable Li-O_2 Batteries. *Adv. Mater.* **2013**, *25*, 5668−5672.
(39) Huang, S.; Fan, W.; Guo, X.; Meng, F.; Liu, X. Positive Role of Surface Defects on Carbon Nanotube Cathodes in Overpotential and Capacity Retention of Rechargeable Lithium-Oxygen Batteries. *ACS Appl. Mater. Interfaces* **2014**, *6*, 21567−21575.
(40) Kichambare, P.; Rodrigues, S.; Kumar, J. Mesoporous Nitrogen-Doped Carbon-Glass Ceramic Cathodes for Solid-State Lithium-Oxygen Batteries. *ACS Appl. Mater. Interfaces* **2012**, *4*, 49−52.
(41) Jin, C.; Yang, Z.; Cao, X.; Lu, F.; Yang, R. A Novel Bifunctional Catalyst of $Ba_{0.9}Co_{0.5}Fe_{0.4}Nb_{0.1}O_{3-\delta}$ Perovskite for Lithium-Air Battery. *Int. J. Hydrogen Energy* **2014**, *39*, 2526−2530.
(42) Hardin, W. G.; Slanac, D. A.; Wang, X.; Dai, S.; Johnston, K. P.; Stevenson, K. J. Highly Active, Nonprecious Metal Perovskite Electrocatalysts for Bifunctional Metal-Air Battery Electrodes. *J. Phys. Chem. Lett.* **2013**, *4*, 1254−1259.
(43) Jung, J.; Jeong, H. Y.; Kim, M. G.; Nam, G.; Park, J.; Cho, J. Fabrication of $Ba_{0.5}Sr_{0.5}Co_{0.8}Fe_{0.2}O_{3-\delta}$ Catalysts with Enhanced Electrochemical Performance by Removing an Inherent Heterogeneous Surface Film Layer. *Adv. Mater.* **2015**, *27*, 266−271.
(44) Jin, C.; Cao, X.; Zhang, L.; Zhang, C.; Yang, R. Preparation and Electrochemical Properties of Urchin-like $La_{0.8}Sr_{0.2}MnO_3$ Perovskite Oxide as a Bifunctional Catalyst for Oxygen Reduction and Oxygen Evolution Reaction. *J. Power Sources* **2013**, *241*, 225−230.
(45) Risch, M.; Stoerzinger, K. A.; Maruyama, S.; Hong, W. T.; Takeuchi, I.; Yang, S. H. $La_{0.8}Sr_{0.2}MnO_{3-\delta}$ Decorated with $Ba_{0.5}Sr_{0.5}Co_{0.8}Fe_{0.2}O_{3-\delta}$: A Bifunctional Surface for Oxygen Electrocatalysis with Enhanced Stability and Activity. *J. Am. Chem. Soc.* **2014**, *136*, 5229−5232.
(46) Zhu, Y.; Zhou, W.; Chen, Z. G.; Chen, Y.; Su, C.; Tade, M. O.; Shao, Z. $SrNb_{0.1}Co_{0.7}Fe_{0.2}O_{3-\delta}$ Perovskite as a Next-Generation Electrocatalyst for Oxygen Evolution in Alkaline Solution. *Angew. Chem., Int. Ed.* **2015**, *54*, 3897−3901.
(47) Zhang, J.; Wang, L.; Xu, L.; Ge, X.; Zhao, X.; Lai, M.; Liu, Z.; Chen, W. Porous Cobalt-Manganese Oxide Nanocubes Derived from Metal Organic Frameworks as a Cathode Catalyst for Rechargeable Li-O_2 Batteries. *Nanoscale* **2015**, *7*, 720−726.
(48) Petrov, A. N.; Kononchuk, O. F.; Andreev, A. V.; Cherepanov, V. A.; Kofstad, P. Crystal Structure, Electrical and Magnetic Properties of $La_{1-x}Sr_xCoO_{3-y}$. *Solid State Ionics* **1995**, *80*, 189−199.
(49) Li, J.; Zhao, Y.; Zou, M.; Wu, C. X.; Huang, Z.; Guan, L. An Effective Integrated Design for Enhanced Cathodes of Ni Foam-Supported Pt/Carbon Nanotubes for Li-O_2 Batteries. *ACS Appl. Mater. Interfaces* **2014**, *6*, 12479−12485.
(50) Zhang, J.; Zhao, Y.; Zhao, X.; Liu, Z.; Chen, W. Porous Perovskite $LaNiO_3$ Nanocubes as Cathode Catalysts for Li-O_2 Batteries with Low Charge Potential. *Sci. Rep.* **2014**, *4*, 6005−6010.

DOI: 10.1021/acsami.5b06587
ACS Appl. Mater. Interfaces 2015, 7, 22478−22486